

# Segmentation of the Blood Vessels and Optic Disk in Retinal Images

Ana Salazar-Gonzalez, Djibril Kaba, Yongmin Li, and Xiaohui Liu

**Abstract**—Retinal image analysis is increasingly prominent as a noninvasive diagnosis method in modern ophthalmology. In this paper, we present a novel method to segment blood vessels and optic disk in the fundus retinal images. The method could be used to support noninvasive diagnosis in modern ophthalmology since the morphology of the blood vessel and the optic disk is an important indicator for diseases like diabetic retinopathy, glaucoma, and hypertension. Our method takes as first step the extraction of the retina vascular tree using the graph cut technique. The blood vessel information is then used to estimate the location of the optic disk. The optic disk segmentation is performed using two alternative methods. The Markov random field (MRF) image reconstruction method segments the optic disk by removing vessels from the optic disk region, and the compensation factor method segments the optic disk using the prior local intensity knowledge of the vessels. The proposed method is tested on three public datasets, DIARETDB1, DRIVE, and STARE. The results and comparison with alternative methods show that our method achieved exceptional performance in segmenting the blood vessel and optic disk.

**Index Terms**—Graph cut segmentation, optic disk segmentation, retinal images, vessel segmentation.

## I. INTRODUCTION

THE segmentation of retinal image structures has been of great interest because it could be used as a noninvasive diagnosis in modern ophthalmology. The morphology of the retinal blood vessel and the optic disk is an important structural indicator for assessing the presence and severity of retinal diseases such as diabetic retinopathy, hypertension, glaucoma, hemorrhages, vein occlusion, and neovascularization. However, to assess the diameter and tortuosity of the retinal blood vessel or the shape of the optic disk, manual planimetry has commonly been used by ophthalmologists, which is generally time consuming and prone to human error, especially when the vessel structures are complicated or a large number of images are acquired to be labeled by hand. Therefore, a reliable automated method for retinal blood vessel and optic disk segmentation,

which preserves various vessel and optic disk characteristics, is attractive in computer-aided diagnosis.

An automated segmentation and inspection of retinal blood vessel features such as diameter, color, and tortuosity as well as the optic disk morphology allows ophthalmologists and eye care specialists to perform mass vision screening exams for early detection of retinal diseases and treatment evaluation. This could prevent and reduce vision impairments, age-related diseases, and many cardiovascular diseases, as well as reduce the cost of the screening.

Over the past few years, several segmentation techniques have been employed for the segmentation of retinal structures such as blood vessels and optic disks and diseases like lesions in fundus retinal images. However, the acquisition of fundus retinal images under different conditions of illumination, resolution and field of view (FOV), and the overlapping tissue in the retina cause a significant degradation of the performance of automated blood vessels and optic disk segmentations. Thus, there is a need for a reliable technique for retinal vascular tree extraction and optic disk detection, which preserves various vessel and optic disk shapes. In the following segment, we briefly review the previous studies on the blood vessel segmentation and optic disk segmentation separately.

## II. RELATED WORKS

Two different approaches have been deployed to segment the vessels of the retina: the pixel-processing-based methods and tracking-based methods [1].

The pixel-processing-based approach performs the vessel segmentation in a two-pass operation. First, the appearance of the vessel is enhanced using detection processes such as morphological preprocessing techniques and adaptive filtering. The second operation is the recognition of the vessel structure using thinning or branch-point operations to classify a pixel as a vessel or background (Bg). These approaches process every pixel in the image and apply multiple operations on each pixel. Some pixel processing methods use neural networks and frequency analysis to define pixels in the image as vessel pixels and Bg pixels. Typical pixel processing operations are shown by Hoover *et al.* [2], Mendoca *et al.* [3], Soares *et al.* [4], Staal *et al.* [5], Chaudhuri *et al.* [6], and Zana *et al.* [7].

The second set of approaches for vessel segmentation are referred to as vessel tracking, vectorial tracking, or tracing [1]. In contrast to the pixel-processing-based approaches, the tracking methods detect first initial vessel seed points, and then track the rest of the vessel pixels through the image by measuring the continuity proprieties of the blood vessels. This technique is used as a single-pass operation, where the detection of the vessel

Manuscript received August 21, 2013; revised January 16, 2014 and November 28, 2013; accepted January 17, 2014. Date of publication January 27, 2014; date of current version November 3, 2014.

A. Salazar-Gonzalez was with the Department of Computer Science, Brunel University, Middlesex, UB8 3PH, London, U.K. She is now with Access IS, Reading, RG6 1AZ, U.K.

D. Kaba, Y. Li, and X. Liu are with the Department of Computer Science, Brunel University, Middlesex, UB8 3PH, London, U.K. (e-mail: kabadjibril@gmail.com).

Color versions of one or more of the figures in this paper are available online at <http://ieeexplore.ieee.org>.

Digital Object Identifier 10.1109/JBHI.2014.2302749

structures and the recognition of the structures are simultaneously performed.

The tracking-based approaches included semiautomated tracing and automated tracing. In the semiautomated tracing methods, the user manually selects the initial vessel seed point. These methods are generally used in quantitative coronary angiography analysis and they generally provide accurate segmentation of the vessels. In fully automated tracing, the algorithms automatically select the initial vessel points and most methods use Gaussian functions to characterize a vessel profile model, which locates a vessel point for the vessel tracing. They are computationally efficient and more suitable for retinal image processing. Examples of the tracking-based approaches are presented by Xu *et al.* [8], Maritiner-perez *et al.* [9], Staal *et al.* [5], and Zhou *et al.* [10].

Both pixel processing and tracking approaches have their own advantages and limitations over each other. The pixel processing approaches can provide a complete extraction of the vascular tree in the retinal image since they search all the possible vessel pixels across the whole image. However, these techniques are computationally expensive and require special hardware to be suitable for large image dataset. The presence of noise and lesions in some retinal images causes a significant degradation in the performance of the pixel processing approaches as the enhancement operation may pick up some noise and lesions as vessel pixels. This could lead to false vessel detection in the recognition operation. On the other hand, the tracking approaches are computationally efficient and much faster than the pixel processing methods because they perform the vessel segmentation using only the pixels in the neighborhood of the vessels structure and avoid the processing of every pixel in the image. Nevertheless, these methods lack in extracting a complete vascular tree in the case where there are discontinuities in the vessel branches. Furthermore, the semiautomated tracking segmentation methods need manual input, which requires time.

The optic nerve head is described as the brightest round area in the retina where the blood vessels converge with a shape that is approximately elliptical and has a width of  $1.8 \pm 0.2$  mm and height  $1.9 \pm 0.2$  mm [11]. The convergence feature of blood vessels into the optic disk region is generally used to estimate the location of the optic disk and segment it from the retinal image. But the intrusion of vessels in the optic disk region constitutes computational complexity for the optic disk segmentation as it is breaking the continuity of its boundary. To address this problem, several methods have been employed such as those presented by Chrastek *et al.* [12], Lowell *et al.* [13], Welfer *et al.* [14], and Aquino *et al.* [15].

Chrastek *et al.* [12] presented an automated segmentation of the optic nerve head for diagnosis of glaucoma. The method removes the blood vessel by using a distance map algorithm; then, the optic disk is segmented by combining a morphological operation, Hough transform, and an anchored active contour model. Lowell *et al.* [13] proposed a deformable contour model to segment the optic nerve head boundary in low-resolution retinal images. The approach localizes the optic disk using a specialized template matching and a directionally sensitive gradient to eliminate the obstruction of the vessel in the optic disk

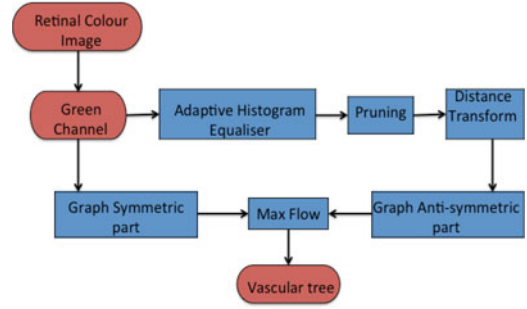


Fig. 1. Vessel segmentation algorithm.

region before performing the segmentation. Welfer *et al.* [14] proposed an automated segmentation of the optic disk in color eye fundus image using an adaptive morphological operation. The method uses a watershed transform marker to define the optic disk boundary, and the vessel obstruction is minimized by morphological erosion.

These techniques are performed using morphological operations to eliminate the blood vessels from the retinal image. However, the application of morphological operations can modify the image by corrupting some useful information.

In our optic disk segmentation process, the convergence feature of vessels into the optic disk region is used to estimate its location. We then use two automated methods [Markov random field (MRF) image reconstruction and compensation factor] to segment the optic disk.

The rest of the paper is organized as follows. The blood vessel segmentation is discussed in Section III. Section IV provides the detailed description of the optic disk segmentation. Section V presents the experimental results of our method with comparisons to other methods. Conclusions are drawn in Section VI. The preliminary results of the three components of the approach, namely the blood vessel segmentation, optic disk segmentation using the graph cut and MRF, respectively, were presented separately in [16]–[18]. More details of the approach can be found in the Ph.D. thesis [19].

### III. BLOOD VESSEL SEGMENTATION

Blood vessels can be seen as thin elongated structures in the retina, with variation in width and length. In order to segment the blood vessel from the fundus retinal image, we have implemented a preprocessing technique, which consists of an effective adaptive histogram equalization and robust distance transform. This operation improves the robustness and the accuracy of the graph cut algorithm. Fig. 1 shows the illustration of the vessel segmentation algorithm.

#### A. Preprocessing

We apply a contrast enhancement process to the green channel image similar to the work presented in [20]. The intensity of the image is inverted, and the illumination is equalized. The resulting image is enhanced using an adaptive histogram equalizer,

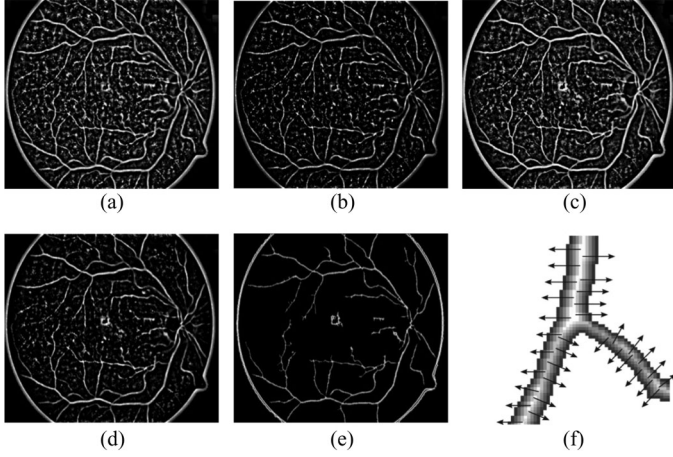


Fig. 2. Preprocessing. (a)  $h = 45, r = 3$ , (b)  $h = 45, r = 6$ , (c)  $h = 81, r = 3$ , (d)  $h = 81, r = 6$ , (e) distance map, and (f) sample of a vessel with arrows indicating the vessel gradients.

given by

$$I_{\text{Enhanced}} = \left( \sum_{p' \in R(p)} \frac{s(I(p) - I(p'))}{h^2} \right)^r \cdot M \quad (1)$$

where  $I$  is the green channel of the fundus retinal color image,  $p$  denotes a pixel, and  $p'$  is the neighborhood pixel around  $p$ .  $p' \in R(p)$  is the square window neighborhood with length  $h$ .  $s(d) = 1$  if  $d > 0$ , and  $s(d) = 0$  otherwise with  $d = s(I(p) - I(p'))$ .  $M = 255$  value of the maximum intensity in the image.  $r$  is a parameter to control the level of enhancement. Increasing the value of  $r$  would also increase the contrast between vessel pixels and the Bg as seen in Fig. 2. The experimental values of the window length was set to  $h = 81$  and  $r = 6$ .

A binary morphological open process is applied to prune the enhanced image, which discards all the misclassified pixels in Fig. 2(d). This approach significantly reduces the false positive, since the enhanced image will be used to construct the graph for segmentation.

A distance map image is created using the distance transform algorithm. This is used to calculate the direction and the magnitude of the vessel gradient. Fig. 2(e) and (f) shows the distance map of the whole image and a sample vessel with arrows indicating the direction of the gradients, respectively. From the sample vessel image, we can see the center line with the brightest pixels, which are progressively reduced in intensity in the direction of the edges (image gradients). The arrows in Fig. 2(f) are referred to as vector field, which are used to construct the graph in the next sections.

### B. Graph Construction for Vessel Segmentation

The graph cut is an energy-based object segmentation approach. The technique is characterized by an optimization operation designed to minimize the energy generated from a given image data. This energy defines the relationship between neighborhood pixel elements in an image.

TABLE I  
WEIGHT ASSIGNMENT OF THE EDGES IN THE GRAPH

Edge	weight	for
$\{p, q\}$	$B_{\{p, q\}}$	$\{p, q\} \in N$
$\{p, S\}$ (Foreground)	$\lambda \cdot R_p(Fg)$ $K$ $0$	$p \in P, p \notin F \cup B$ $p \in F$ $p \in B$
$\{p, T\}$ (Background)	$\lambda \cdot R_p(Bg)$ $0$ $K$	$p \in P, p \notin F \cup B$ $p \in F$ $p \in B$

A graph  $G(\nu, \epsilon)$  is defined as a set of nodes (pixels)  $\nu$  and a set of undirected edges  $\epsilon$  that connect these neighboring nodes. The graph included two special nodes, a foreground (Fg) terminal (source  $S$ ) and a Bg terminal (sink  $T$ ).  $\epsilon$  includes two types of undirected edges: neighborhood links ( $n$ -links) and terminal links ( $t$ -links). Each pixel  $p \in P$  (a set of pixels) in the graph presents two  $t$ -links  $\{p, S\}$  and  $\{p, T\}$  connecting it to each terminal, while a pair of neighboring pixels  $\{p, q\} \in N$  (number of pixel neighbors) is connected by an  $n$ -link [21]. Thus,

$$\epsilon = N \bigcup_{p \in P} \{\{p, S\}, \{p, T\}, \nu = P \cup \{S, T\}\}. \quad (2)$$

An edge  $e \in \epsilon$  is assigned a weight (cost)  $W_e > 0$ . A cut is defined by a subset of edges  $C \in \epsilon$ , where  $G(c) = (\nu, \epsilon \setminus C)$  separating the graph into Fg and Bg with  $C$  defined as  $|C| = \sum_{e \in C} W_e$ .

The max-flow algorithm is used to cut the graph and find the optimal segmentation. Table I assigns weight to the edges  $\epsilon$  in the graph [21], where

$$K = 1 + \max_{p \in P} \sum_{\{p, q\}} B_{p, q}, \quad (3)$$

and  $F$  and  $B$  represent the subsets of pixels selected as the Fg and Bg, respectively. Thus,  $F \subset P$  and  $B \subset P$  such that  $F \cap B = \emptyset$ .  $B_{p, q}$  defines the discontinuity between neighboring pixels, and its value is large when the pixel intensities.  $\lambda > 0$  is a constant coefficient, which we will define in the energy formulation of the graph.

The graph cut technique is used in our segmentation because it allows the incorporation of prior knowledge into the graph formulation in order to guide the model and find the optimal segmentation. Let us assume  $A = (A_1, A_p, \dots, A_P)$  is a binary vector set of labels assigned to each pixel  $p$  in the image, where  $A_p$  indicate assignments to pixels  $p$  in  $P$ . Therefore, each assignment  $A_p$  is either in the Fg or Bg. Thus, the segmentation is obtained by the binary vector  $A$  and the constraints imposed on the regional and boundary proprieties of vector  $A$  are derived by the energy formulation of the graph defined as

$$E(A) = \lambda \cdot R(A) + B(A) \quad (4)$$

where the positive coefficient  $\lambda$  indicates the relative importance of the regional term (likelihoods of Fg and Bg)  $R_A$  against the boundary term (relationship between neighborhood pixels)  $B_A$ . The regional or the likelihood of the Fg and Bg is given by

$$R(A) = \sum_{p \in P} R_p(A_p) \quad (5)$$



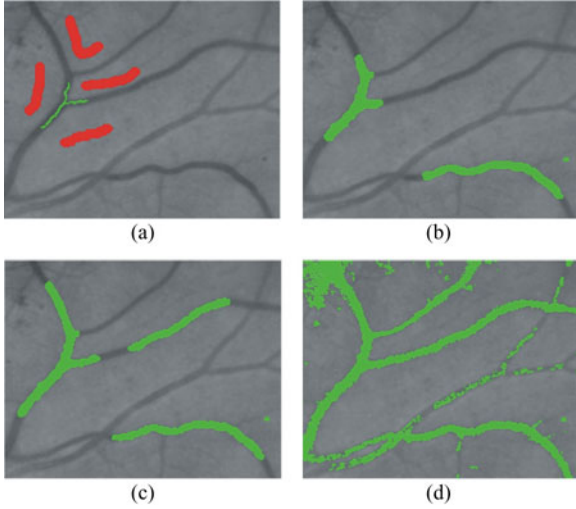


Fig. 3. Retinal blood vessel segmentation using the traditional graph. (a) Seeds initialization of the input image, (b)  $\lambda = 20$ , (c)  $\lambda = 50$ , and (d)  $\lambda = 100$ .

and the boundary constraints are defined as

$$B(A) = \sum_{p,q \in N} B_{p,q} \cdot \phi(A_p, A_q) \quad (6)$$

where  $\phi(A_p, A_q) = 1$  for  $A_p \neq A_q$  and 0 otherwise,

$$B_{p,q} = \exp\left(-\frac{(I_p - I_q)^2}{2\sigma^2}\right) \cdot \frac{1}{\text{dist}(p, q)}. \quad (7)$$

$R_p(A_p)$  specifies the assignment of pixel  $p$  to either the Fg or the Bg.  $B_{p,q}$  defines the discontinuity between neighboring pixels, and its value is large when the pixel intensities  $I_p$  and  $I_q$  are similar and close to zero when they are different. The value of  $B_{p,q}$  is also affected by the Euclidean distance  $\text{dist}(p, q)$  between pixels  $p$  and  $q$ .

During the minimization of the graph energy formulation in (4) to segment thin objects like blood vessels, the second term (boundary term) in (4) has a tendency to follow short edges known as “the shrinking bias” [22]. This problem causes a significant degradation of the performance of the graph cut algorithm on thin elongated structures like the blood vessels. Fig. 3 shows an example of the blood vessel segmentation using the traditional graph formulation [23]. From Fig. 3, it can be seen that the blood vessel segmentation follows short edges, and tends to shrink in the search for the cheapest cost. It can also be noticed that  $\lambda$  in (4) controls the relation between the boundary and regional terms. Increasing the value of  $\lambda$ , the likelihood of the pixels belonging to the Fg and Bg ( $t$ -links) gains strength over the regional term ( $n$ -links), which slightly improves the segmentation result as shown in Fig. 3(d).

To address the aforementioned problem, the segmentation of blood vessels using the graph cut requires a special graph formulation. One of the methods used to address the shrinking bias problem is to impose an additional connectivity prior, where the user marks the constraint connectivity [22]. In order to achieve full automated segmentation, we used the method presented in [23], which overcomes the “shrinking bias” by adding the mechanism of vectors flux into the construction of the graph.

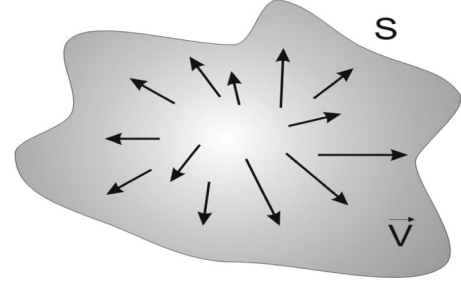


Fig. 4. Flux of vectors  $\mathbf{v}$  passing through a given surface  $S$ .

The incorporation of vectors flux can improve edge alignment and allows the segmentation of thin objects like blood vessels by keeping a balance between shrinking (length) and stretching (vectors flux) along the boundary. Fig. 4 shows a flux of vectors  $\mathbf{v}$  passing through a given surface  $S$ . Our method takes the image gradients of rough blood vessels from the preprocessing step as vectors  $\mathbf{v}$  shown in Fig. 2(f), and the flux (magnitude and direction) of these vectors is incorporated into the graph construction and optimized. Thus, the shrinking effect of the minimization energy on the boundary term is equilibrated with the spreading effect of vectors  $\mathbf{v}$  flux.

It has been shown in [23] that the class of the Finsler metrics can describe geometric proprieties of the discrete cut metric on regular grids and the Finsler length can be represented by the sum of two terms. Those terms represent the symmetric and antisymmetric parts of the cut metric. The symmetric part of the cut defines the standard geometric length of contour and it is independent of its orientation. The antisymmetric part of the cut metric represents the flux of a given vector field through the contour [23].

To address “the shrinking bias” problem shown in Fig. 3, we have constructed a graph consisting of a symmetric part  $g^+$  (shrinking) and an antisymmetric part  $g^-$  (stretching) by incorporating the flux of vector  $\mathbf{v}$  into the graph construction. The symmetric part  $g^+$  of the graph corresponds to a cut geometric length and is related directly to the  $n$ -link connections and the antisymmetric part  $g^-$  is equal to the flux of the vector field  $\mathbf{v}$  over the cut geometric and it is used to derive the  $t$ -links. Thus, the blood vessels can be segmented by keeping a good balance between shrinking and stretching (flux) throughout the image boundary.

*1) Symmetric Part of the Graph:* It is used to assign weights on the  $n$ -link connections (edges between neighboring pixels). Let us consider a neighbor system of a graph described by a set of edges  $e_k$ , where  $1 \leq k \leq N$ , for  $N$  number of neighbors. Let us define  $e_k$  as the shortest vector connecting two pixels in the direction of  $k$ ,  $W_k^+(p)$  as the weight of the edge  $e_k$  at pixel  $p$ , and  $\widetilde{W}_k^+(p)$  as a set of the edge weights at pixel  $p$  for all directions. The corresponding edge weights are defined by

$$\omega^+ = \frac{1}{2} D \times g^+ \quad (8)$$

where  $D$  is an  $N \times N$  matrix with entries defined as

$$D_{ii} = -\frac{\sin(\alpha_{i+1} - \alpha_{i-1})}{\sin(\alpha_{i+1} - \alpha_i)\sin(\alpha_i - \alpha_{i-1})} \quad (9)$$

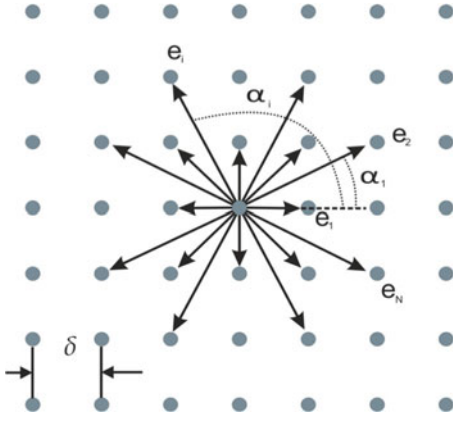


Fig. 5. Neighborhood system for a grid in the graph.

$$D_{ij} = \begin{cases} \frac{1}{\sin(\alpha_j - \alpha_i)} & \text{if } j + 1 \pm 1 \bmod N \\ 0 & \text{for other entries} \end{cases}$$

where  $\alpha_k$  is the angle of the edge  $e_k$  with respect to the positive axis  $X$  as shown in Fig. 5.

In our implementation, we consider a grid map of 16 neighbors with edges  $e_k, k = 1, 2, \dots, 16$  as shown in Fig. 5. For each pixel  $p$  in the green channel image, the edge weight  $\tilde{W}_k^+(p)$  is computed according to (8).  $g^+$  is calculated using the pixel intensity difference between two given nodes by

$$g^+ = K \cdot \exp\left(\frac{-(I_p - I_q)^2}{\sigma^2}\right). \quad (10)$$

$g^+$  has a high value for pixels of similar intensities, when  $I_p - I_q < \sigma$ . However, if the pixels are very different  $I_p - I_q > \sigma$ , the value of  $g^+$  is small, which represents a poor relation between the pixels; hence, they belong to different terminals [24].

2) *Antisymmetric Part of the Graph:* We used the term antisymmetry because the flux (stretching) of the vector field  $\mathbf{v}$  over the cut geometric balanced the shrinking of blood vessels during the segmentation. This antisymmetric part of the graph is defined by the flux of the vector field  $\mathbf{v}$  over the cut geometric. It is used to assign weights on the  $t$ -links (edges between a given pixel and the terminals) to balance the shrinking effect seen in Fig. 3. Specific weights for  $t$ -links are obtained based on the deposition of vector  $\mathbf{v}$ . Different decompositions of vector  $\mathbf{v}$  may result in different  $t$ -links whose weights can be interpreted as an estimation of divergence. In our implementation, we decomposed the vector  $\mathbf{v}$  along grid edges with the  $n$ -links oriented along the main axes, i.e., in the  $X$ - and  $Y$ -directions. Thus, vector  $\mathbf{v}$  can be decomposed as  $\mathbf{v} = v_x u_x + v_y u_y$ , where  $u_x$  and  $u_y$  are unit vectors in the  $X$ - and  $Y$ -directions, respectively. This decomposition leads to the  $t$ -link weights defined as

$$t_p = \frac{\delta^2}{2} [(v_x^{\text{right}} - v_x^{\text{left}}) + (v_y^{\text{up}} - v_y^{\text{down}})] \quad (11)$$

where  $v_x^{\text{right}}$  and  $v_x^{\text{left}}$  are the components of vector  $\mathbf{v}$  in the  $X$ -direction taken at the right and left neighbors of pixel  $P$ ,

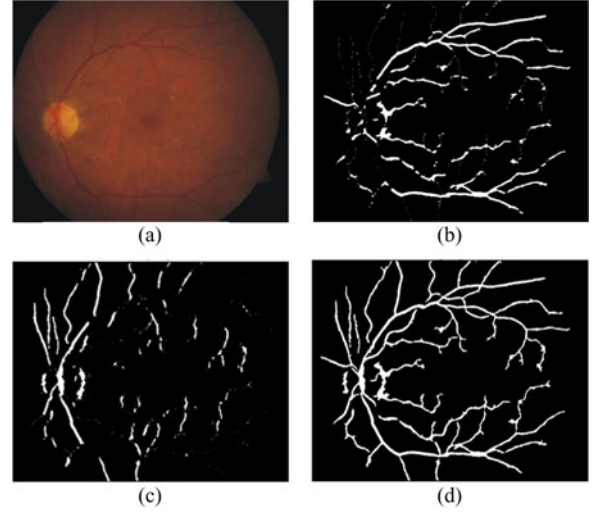


Fig. 6. Vessel segmentation using the decomposition of vector  $\mathbf{v}$ : (a) input retinal image, (b) blood vessel segmentation using horizontal ( $X$ -axis) decomposition of vector  $\mathbf{v}$ , (c) blood vessel segmentation using vertical ( $Y$ -axis) decomposition of vector  $\mathbf{v}$ , and (d) blood vessel segmentation result using the decomposition of vector  $\mathbf{v}$  along the  $X$ - and  $Y$ -axes.

respectively.  $v_y^{\text{up}}$  and  $v_y^{\text{down}}$  are in the  $Y$ -direction of vector  $\mathbf{v}$  taken at the top and down neighbors of pixel  $P$ .  $\delta$  is the size of the cell in the grid map (see Fig. 5). We add edge  $(s \rightarrow p)$  with weight  $C * (-tp)$  if  $tp < 0$ , or edge  $(p \rightarrow t)$  with weight  $C * tp$  otherwise. The parameter  $C$  is related to the magnitude of the vector  $\mathbf{v}$ ; thus, the pixels in the center of the blood vessel have a higher connection to the source (Fig) than the pixels in the edge of the blood vessels. Because the distance map is calculated on the pruned image and vector  $\mathbf{v}$  is only defined for the pixels detected as blood vessels in the rough segmentation, for the rest of the pixels in the image, the initialization of  $t$ -link weights is set as  $(p \rightarrow s)$  with weight  $t = 0$  and  $(p \rightarrow t)$  with weight  $t = K$ , where  $K$  is the maximum weight sum for a pixel in the symmetric construction. Fig. 6 shows the segmentation results of the blood vessels using different decomposition of the vector  $\mathbf{v}$  generating different  $t$ -link weights.

#### IV. OPTIC DISK SEGMENTATION

The optic disk segmentation starts by defining the location of the optic disk. This process used the convergence feature of vessels into the optic disk to estimate its location. The disk area is then segmented using two different automated methods (MRF image reconstruction and compensation factor). Both methods use the convergence feature of the vessels to identify the position of the disk. The MRF method is applied to eliminate the vessel from the optic disk region. This process is known as image reconstruction and it is performed only on the vessel pixels to avoid the modification of other structures of the image. The reconstructed image is free of vessels and it is used to segment the optic disk via graph cut. In contrast to MRF method, the compensation factor approach segments the optic disk using prior local intensity knowledge of the vessels. Fig. 7 shows the overview of both the MRF and the compensation factor methods.

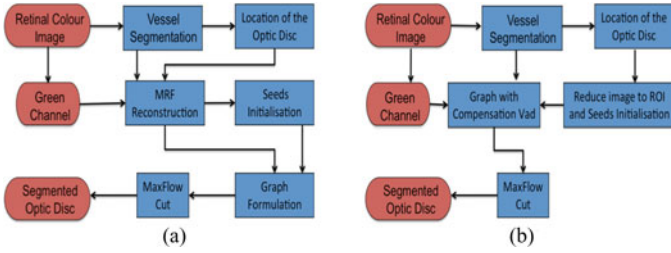


Fig. 7. (a) MRF image reconstruction method diagram and (b) compensation factor method diagram.

#### A. Optic Disk Location

Inspired by the method proposed in [14], which effectively locates the optic disk using the vessels, we use the binary image of vessels segmented in Section III to find the location of the optic disk. The process iteratively traces toward the centroid of the optic disk. The vessel image is pruned using a morphological open process to eliminate thin vessels and keep the main arcade. The centroid of the arcade is calculated using the following formulation:

$$C_x = \sum_{i=1}^K \frac{x_i}{K} \quad C_y = \sum_{i=1}^K \frac{y_i}{K} \quad (12)$$

where  $x_i$  and  $y_i$  are the coordinates of the pixel in the binary image and  $K$  is the number of pixels set to 1 (pixels marked as blood vessels) in the binary image.

Given the gray scale intensity of a retinal image, we select 1% of the brightest region. The algorithm detects the brightest region with the most number of pixels to determine the location of the optic disk with respect to the centroid point (right, left, up, or down). The algorithm adjusts the centroid point iteratively until it reaches the vessel convergence point or the center of the main arcade (center of the optic disk) by reducing the distance from one centroid point to next one in the direction of the brightest region, and correcting the central position inside the arcade accordingly. Fig. 8 shows the process of estimating the location of the optic disk in a retinal image. It is important to notice that the vessel convergence point must be detected accurately, since this point is used to automatically mark Fg seeds. A point on the border of the optic disk may result in some false Fg seeds. After the detection of the vessel convergence point, the image constrained a region of interest (ROI) including the whole area of the optic disk to minimize the processing time. This ROI is set to a square of  $200 \times 200$  pixels concentric with the detected optic disk center. Then, an automatic initialization of seeds (Fg and Bg) for the graph is performed. A neighborhood of 20 pixels of radius around the center of the optic disk area is marked as the Fg pixels, and a band of pixels around the perimeter of the image are selected as the Bg seeds in Fig. 9.

#### B. Optic Disk Segmentation With MRF Image Reconstruction

The high contrast of blood vessels inside the optic disk presented the main difficulty for its segmentation as it misguides the segmentation through a short path, breaking the continuity of the optic disk boundary. To address this problem, the MRF-

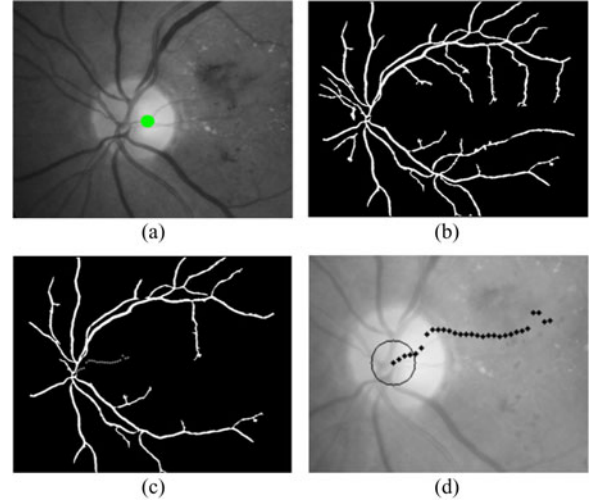


Fig. 8. Optic disk detection. (a) Retinal image green channel with 1% of the brightest region selected in green color, (b) binary segmented blood vessel, (c) binary segmented blood vessel after pruning, and (d) sequence of points from the centroid to vessel convergence point (optic disk location).

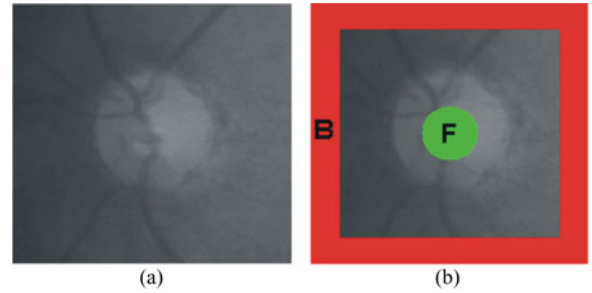


Fig. 9. Optic disk detection. (a) ROI image, (b) initialization of the foreground F, and the background B of the ROI image.

based reconstruction method presented in [25] is adapted in our study. We have selected this approach because of its robustness. The objective of our algorithm is to find a best match for some missing pixels in the image; however, one of the weaknesses of the MRF-based reconstruction is the requirement of intensive computation. To overcome this problem, we have limited the reconstruction to the ROI, and using prior segmented retina vascular tree, the reconstruction was performed in the ROI. An overview diagram of the optic disk segmentation with the MRF image reconstruction is shown in Fig. 7.

Let us consider a pixel neighborhood  $w(p)$  defined as a square window of size  $W$ , where pixel  $p$  is the center of the neighborhood.  $I$  is the image to be reconstructed and some of the pixels in  $I$  are missing. Our objective is to find the best approximate values for the missing pixels in  $I$ . So, let  $d(w_1, w_2)$  represent a perceptual distance between two patches that defines their similarity. The exact matching patch corresponds to  $d(w', w(p)) = 0$ . If we define a set of these patches as  $\Omega(p) = \{\omega' \subset I : d(\omega', \omega(p)) = 0\}$ , the probability density function of  $p$  can be estimated with a histogram of all center pixel values in  $\Omega(p)$ . However, since we are considering a finite neighborhood for  $p$  and the searching is limited to the image area, there might not be any exact matches for a patch. For



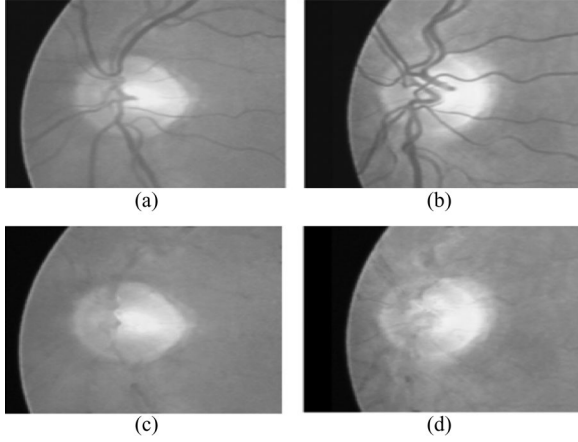


Fig. 10. MRF reconstruction applied to retinal images. Top: original gray-scale images. Bottom: reconstructed images using the MRF-based method.

this reason, we find a collection of patches, whose match falls between the best match and a threshold. The closest match is calculated as  $\omega_{\text{best}} = \text{argmin}_{\omega} d(\omega(p), \omega) \subset I$ . All the patches  $\omega$  with  $d(\omega(p), \omega) < (1 + \epsilon)d(\omega(p), \omega_{\text{best}})$  are included in the collection  $\omega'$ .  $d(\omega', \omega(p))$  is defined as the sum of the absolute differences of the intensities between patches, so identical patches will result in  $d(\omega', \omega(p)) = 0$ . Using the collection of patches, we create a histogram and select the one with the highest mode. Fig. 10 shows sample results of the reconstruction. The  $\text{Fg}_s$  and the  $\text{Bg}_s$  seeds are initialized in the reconstructed image, which are then used in graph cut formulation to segment the optic disk. Similar to Fig. 9, the initialization of the  $\text{Fg}_s$  and  $\text{Bg}_s$  seeds is performed using the reconstructed image.

The graph cut algorithm described in Section III-B is used to separate the Fg and the Bg by minimizing the energy function over the graph and producing the optimal segmentation of the optic disk in the image. The energy function of the graph in (4) consists of regional and boundary terms. The regional term (likelihoods of Fg and Bg) is calculated using (5), while the boundary term (relationship between neighboring pixels) is derived using (6). A grid of 16 neighbors  $N$  is selected to create links between pixels in the image  $Im$ . The max-flow algorithm is used to cut the graph and find the optimal segmentation.

### C. Optic Disk Segmentation With a Compensation Factor

In contrast to the MRF image reconstruction, we have incorporated the blood vessels into the graph cut formulation by introducing a compensation factor  $V_{ad}$ . This factor is derived using prior information of the blood vessel.

The energy function of the graph cut algorithm generally comprises boundary and regional terms. The boundary term defined in (6) is used to assign weights on the edges ( $n$ -links) to measure the similarity between neighboring pixels with respect to the pixel properties (intensity, texture, and color). Therefore, pixels with similar intensities have a strong connection. The regional term in (5) is derived to define the likelihood of the pixel belonging to the Bg or the Fg by assigning weights on the edges ( $t$ -link) between the image pixels and the two terminals

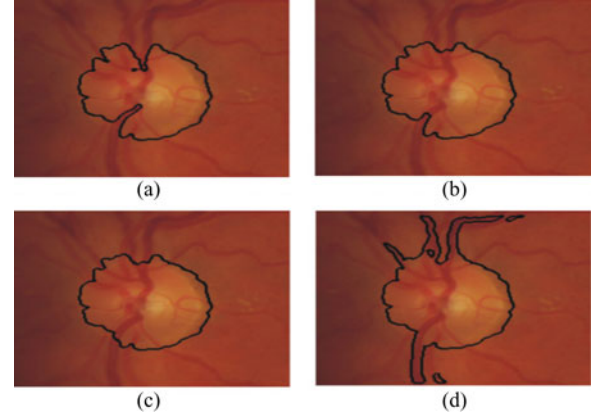


Fig. 11. Optic disk segmentation with the compensation factor  $V_{ad}$  method: (a)  $V_{ad} = 20$ , (b)  $V_{ad} = 100$ , (c)  $V_{ad} = 150$ , and (d)  $V_{ad} = 250$ .

Bg and Fg seeds. In order to incorporate the blood vessels into the graph cut formulation, we derived the  $t$ -link as follows:

$$S_{\text{link}} = \begin{cases} -\ln P_r(I_p \setminus \text{Fg}_{\text{seeds}}) & \text{if } p \neq \text{vessel} \\ -\ln P_r(I_p \setminus \text{Fg}_{\text{seeds}}) + V_{ad} & \text{if } p = \text{vessel} \end{cases} \quad (13)$$

$$T_{\text{link}} = \begin{cases} -\ln P_r(I_p \setminus \text{Bg}_{\text{seeds}}) & \text{if } p \neq \text{vessel} \\ -\ln P_r(I_p \setminus \text{Bg}_{\text{seeds}}) & \text{if } p = \text{vessel} \end{cases} \quad (14)$$

where  $p$  is the pixel in the image,  $\text{Fg}_{\text{seeds}}$  is the intensity distribution of the Fg seeds,  $\text{Bg}_{\text{seeds}}$  represents the intensity distribution of the Bg seeds, and  $V_{ad}$  is the compensation factor given as

$$V_{ad} = \max_{p \in \text{vessel}} \{-\ln P_r(I_p \setminus \text{Bg}_{\text{seeds}})\}. \quad (15)$$

The intensity distribution of the blood vessel pixels in the region around the optic disk makes them more likely to belong to Bg pixels than the Fg (or the optic disk pixels). Therefore, the vessels inside the disk have weak connections with neighboring pixels making them likely to be segmented by the graph cut as Bg. We introduce in (13) a compensation vector to all  $t$ -links of the Fg for pixels belonging to the vascular tree to address this behavior. Consequently, vessels inside the optic disk are classified with respect to their neighborhood connections instead of their likelihood with the terminals Fg and Bg seeds. Fig. 11 shows sample of images segmented by the compensation factor. The segmentation of the disk is affected by the value of  $V_{ad}$ , and the method achieves poor segmentation results for low value of  $V_{ad}$ . However, when the value of the  $V_{ad}$  increases, the performance improves until the value of  $V_{ad}$  is high enough to segment the rest of the vessels as Fg.

## V. RESULTS

For the vessel segmentation method, we tested our algorithm on two public datasets, DRIVE [5] and STARE [2] with a total of 60 images. The optic disk segmentation algorithm was tested on DRIVE [5] and DIARETDB1 [26], consisting of 129 images in total. The performances of both methods are tested against a number of alternative methods.

The DRIVE consists of 40 digital images which were captured from a Canon CR5 nonmydriatic 3CCD camera at  $45^\circ$  FOV. The images have a size of  $768 \times 584$  pixels. The dataset includes

masks to separate the FOV from the rest of the image. It included two sets of hand-labeled images (set A and set B) for the blood vessel. Set A offers the manually labeled images for all the images in the dataset, whereas set B provides the manually labeled images for half of the dataset. To test our method, we adopt the set A hand labeling as the benchmark. We manually delimited the optic disk to test the performance of the optic disk segmentation algorithm.

The STARE dataset consists of 20 images captured by a Top-Con TRV-50 fundus camera at 35° FOV. The size of the images is  $700 \times 605$  pixels. We calculated the mask image for this dataset using a simple threshold technique for each color channel. The STARE dataset included images with retinal diseases selected by Hoover *et al.* [2]. It also provides two sets of hand-labeled images performed by two human experts. The first expert labeled fewer vessel pixels than the second one. To test our method, we adopt the first expert hand labeling as the ground truth.

The DIARETDB1 dataset consists of 89 color images with 84 of them containing at last one indication of lesion. The images were captured with a digital fundus camera at 50° FOV and had a size of  $1500 \times 1152$  pixels. Hand-labeled lesion regions are provided in this dataset by four human experts. However, the DIARETDB1 dataset only includes the hand-labeled ground truth of lesions but not the blood vessels and the optic disk. For this reason, we were unable to compare the performance of the blood vessel segmentation on the DIARETDB1 dataset. Nevertheless, we were able to create the hand-labeled ground truth of an optic disk to test the performance of the optic disk segmentation.

To facilitate the performance comparison between our method and alternative retinal blood vessels segmentation approaches, parameters such as the true positive rate (TPR), the false positive rate (FPR), and the accuracy rate (ACC) are derived to measure the performance of the segmentation [5]. The ACC is defined as the sum of the true positives (pixels correctly classified as vessel points) and the true negatives (nonvessel pixels correctly identified as nonvessel points), divided by the total number of pixels in the images. The TPR is defined as the total number of true positives, divided by the number of blood vessel pixels marked in the ground true image. The FPR is calculated as the total number of false positives divided by the number of pixels marked as nonvessel in the ground true image. It is worth mentioning that a perfect segmentation would have an FPR of 0 and a TPR of 1. Our method and all the alternative methods used the first expert hand-labeled images as a performance reference.

Most of the alternative methods use the whole image to measure the performance. In [5], all the experiments are carried out on the FOV without considering the performance in the dark area outside the FOV. The method in [3] measures the performance on both the whole image and the FOV. The dark Bg outside the FOV in the retinal image is easy to segment. It is an advantage in measuring the true negatives pixels when the whole image is considered. We have calculated the percentage of pixels outside the FOV in the images for the two datasets, which represents approximately 25% of the pixels in the whole image. However, it does not affect all the measurement metrics, except when the true negative value is involved (e.g., ACC). On

TABLE II  
PERFORMANCE COMPARISON IN THE STARE DATASET

Method	TPR	FPR	Accuracy
$2^{nd}$ human expert [9]	0.8951	0.0438	0.9522
Hoover[2]	0.6751	0.0433	0.9267
Staal[5]	0.6970	0.0190	0.9541
Mendonca[3]	0.6996	0.0270	0.9440
Martinez[9]	0.7506	0.0431	0.9410
Chaudhuri[6]	0.6134	0.0245	0.9384
Kaba [27]	0.6645	0.0216	0.9450
Zhang [29]	0.7177	0.0247	0.9484
Marin [28]	-	-	0.9526
<b>Our method</b>	0.7887	0.0367	0.9441

TABLE III  
PERFORMANCE COMPARISON OF HEALTHY VERSUS DISEASE IMAGES  
IN THE STARE DATASET

Heathy images			
Method	TPR	FPR	Accuracy
Mendonca[3]	0.7258	0.0209	0.9492
Hoover[2]	0.6766	0.0338	0.9324
Chaudhuri[6]	0.7335	0.0218	0.9486
Zhang [29]	0.7526	0.0221	0.9510
Soares [30]	0.7554	0.0188	0.9542
<b>Our method</b>	0.8717	0.0364	0.9513
Unhealthy images			
Method	TPR	FPR	Accuracy
Mendonca[3]	0.6733	0.0331	0.9388
Hoover[2]	0.6736	0.0528	0.9211
Chaudhuri[6]	0.5881	0.0384	0.9276
Zhang [29]	0.7166	0.0327	0.9439
Soares [30]	0.6869	0.0318	0.9416
<b>Our method</b>	0.7057	0.0371	0.9369

the other hand, most of the methods use the whole image to measure their performance, making the comparison fair.

#### A. Results of the Blood Vessel Segmentation Algorithm on the STARE Dataset

Tables II and III show performance comparison results of our approach with recent alternative methods in terms of TPR, FPR, and ACC on the STARE dataset. The performance results of the second expert hand labeled and the method proposed by Martinez-Perez *et al.* [9] and Staal *et al.* [5] are taken from [9]. The results of the methods proposed by Mendonca *et al.* [3] and Hoover *et al.* [2] are taken from [3], and the approaches of Chaudhuri *et al.* [6], Kaba *et al.* [27] Marin *et al.* [28], and Zhang *et al.* [29] were generated from their original manuscripts. The performance results of segmentation for Zhang *et al.* [29], Chaudhuri *et al.* [6], and Soares *et al.* [30] on both healthy and



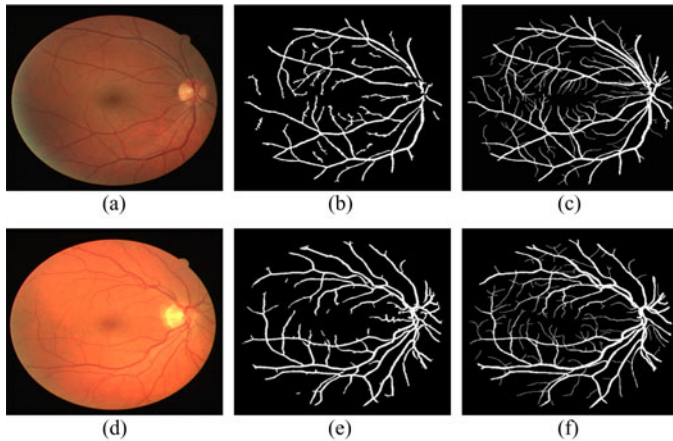


Fig. 12. DRIVE dataset: (a) and (d) retinal images, (b) and (e) our segmentation results, and (c) and (f) manually labeled results.

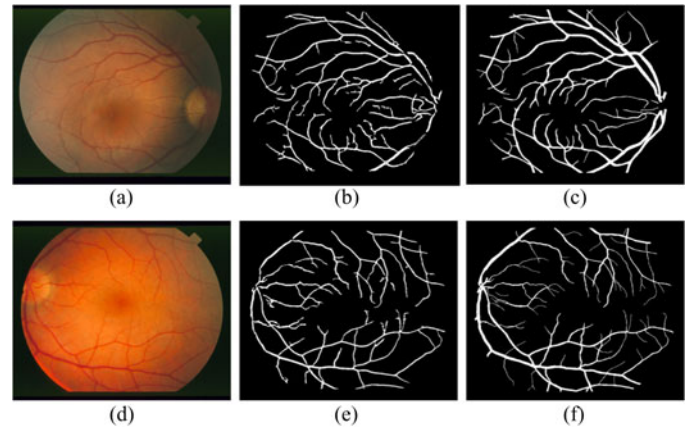


Fig. 13. STARE dataset: (a) and (d) retinal images, (b) and (e) our segmentation results, and (c) and (f) manually labeled results.

unhealthy images were taken from [29]. The testing includes all the 20 fundus images except the method proposed by Staal *et al.* [5] which used 19 out of the 20 (ten healthy and nine unhealthy) images.

In Table II, the second human expert hand-labeled image is considered as the target performance level with average  $TPR = 0.7887$ , given the first human expert hand-labeled image as benchmark. Thus, our method needs an improvement of 10.64% in average true positive, whereas Mendonca *et al.*, Staal *et al.*, Chaudhuri *et al.*, Hoover *et al.*, Kaba *et al.*, Martinez-Perez *et al.*, and Zhang *et al.* have a room of improvement of 19.55%, 19.81%, 28.17%, 22.00%, 23.06%, 14.45%, and 17.74%, respectively.

Considering the value of average TPR as a performance measure, our proposed approach reaches better performance than all the other methods. However, with the average ACC, our method is only marginally inferior to the methods presented by Staal *et al.* [5], Kaba *et al.* [27], Marin *et al.* [28], and Zhang *et al.* [29], but as mentioned previously, Staal *et al.* [5] used 19 of the 20 images. Compared to the methods proposed by Hoover *et al.* [2], Martinez-Perez *et al.* [9], and Chaudhuri *et al.* [6], our approach outperforms the ACC of these techniques and it has approximately the same value of ACC as Mendonca *et al.* [3].

Table III compares the performance of the healthy subject images against the unhealthy subject images on the STARE dataset. The results of the experiments show that the unhealthy ocular images cause a significant degradation of the performance of automated blood vessel segmentation techniques. An overview of the results shows that in both healthy and unhealthy images, our proposed method achieves a better overall average TPR performance than all the other methods. However, the average ACC value is comparable to the performance of Soares *et al.* [30] and Zhang *et al.* [29]. It outperforms the ACC of Mendonca *et al.* [3], Hoover *et al.* [2], and Chaudhuri *et al.* [6] in both healthy and unhealthy images.

Figs. 12 and 13 show the segmented images and the manually labeled images for the DRIVE and the STARE datasets, respectively.

### B. Results of the Blood Vessel Segmentation Algorithm on the DRIVE Dataset

The performance of the segmentation of our method on the DRIVE dataset is compared with alternative methods: Zhang *et al.* [29], Soares *et al.* [30], Zana *et al.* [7], Garg *et al.* [31], Perfetti *et al.* [32], and Al-Rawi *et al.* [33] taken from [29]. The results of the second human expert B and the method proposed by Niemeijer *et al.* [34], Mendonca *et al.* [3], and Staal *et al.* [5] were acquired from [3]. The results of the methods proposed by Cinsdikici *et al.* [35] and Jiang *et al.* [36] were generated from Marin *et al.* [28], and finally, the results of the methods by Ricci *et al.* [37], Soares *et al.* [30], and Martinez-Perez *et al.* [9] were acquired from their original manuscripts.

The second human expert B hand-labeled image [3] is considered as the target performance level with average ( $TPR = 0.7761$  and  $ACC = 0.9473$ ) given the first human expert A hand-labeled image as reference (benchmark). Table IV shows the performance of our method against the aforementioned methods on the DRIVE dataset. Our method needs an overall improvement of 2.49% and 0.61% in average TPR and average ACC, respectively.

On the other hand, with an average TPR of 0.7512, our method achieves better performance than all the other methods with respect to the average TPR value. The average accuracy achieved with our approach on DRIVE outperforms Jiang *et al.* [36], Cinsdikici *et al.* [35], Zana *et al.* [7], Garg *et al.* [31], Zhang *et al.* [29], and Martinez *et al.* [9]. But it is marginally inferior to the methods proposed by Al-Rawi *et al.* [33], Ricci *et al.* [37], and Mendonca *et al.* [3], and it is comparable to Soares *et al.* [30], Marin *et al.* [28], Niemeijer *et al.* [34], and Staal *et al.* [5].

It is important to note that the methods presented by Ricci *et al.* [37], Soares *et al.* [30], Marin *et al.* [28], Niemeijer *et al.* [34], and Staal *et al.* [5] used supervised techniques that generally depend on the training datasets; thus to achieve good results, classifier retraining is required before performing any experimentation on new datasets.

An overview of the testing results on DRIVE shows that our method offers a reliable and robust segmentation solution for

TABLE IV  
PERFORMANCE COMPARISON IN THE DRIVE DATASET

Method	TPR	FPR	Accuracy
Human expert B[3]	0.7761	0.0275	0.9473
Staal[5]	0.7194	0.0227	0.9442
Mendonca[3]	0.7344	0.0236	0.9452
Niemeijer[34]	0.6898	0.0304	0.9417
Jiang[36]	-	-	0.8911
Cinsdikici [35]	-	-	0.9293
Marin [28]	-	-	0.9452
Ricci[37]	-	-	0.9633
Zana[7]	-	-	0.9377
Garg[31]	-	-	0.9361
Perfetti[32]	-	-	0.9261
Al-Rawi[33]	-	-	0.9510
Soares[30]	-	-	0.9466
Zhang[29]	0.7120	0.0276	0.9382
Martinez[9]	0.7246	0.0345	0.9344
<b>Our method</b>	<b>0.7512</b>	<b>0.0316</b>	<b>0.9412</b>

blood vessels. It is clearly observed that our approach reaches better performance in terms of the average TPR.

### C. Results of Optic Disk Segmentation on the DIARETDB1 and DRIVE Datasets

The performance results of our approach are compared to the alternative methods: the adaptive morphological approach by Welfer *et al.* [14], the traditional graph cut technique by Boykov *et al.* [24], and the topology cut technique proposed by Zeng *et al.* [38]. Unfortunately, it was not possible to test our method against a large number of alternative methods, since most of the methods do use a unique benchmark to measure the results of the optic disk segmentation; therefore, this makes the comparison of the results difficult. Further comparison is made between our two optic disk segmentation methods (the compensation factor and the MRF image reconstruction). All the methods are tested on the same datasets (DIARETDB1 and DRIVE) of 109 fundus retinal images in total, including those with a discernable optic disk.

The optic disk segmentation performance is evaluated by the overlapping ratio  $O_{ratio}$  and the mean absolute distance (MAD). The overlapping ratio is defined to measure the common area between the optic disk region in the ground truth and the optic disk region segmented by our method. It is defined by the following formulation:

$$O_{ratio} = \frac{G \cap S}{G \cup S} \quad (16)$$

where  $G$  represents the true optic disk boundary (manually labeled region) and  $S$  is the optic disk boundary segmented by

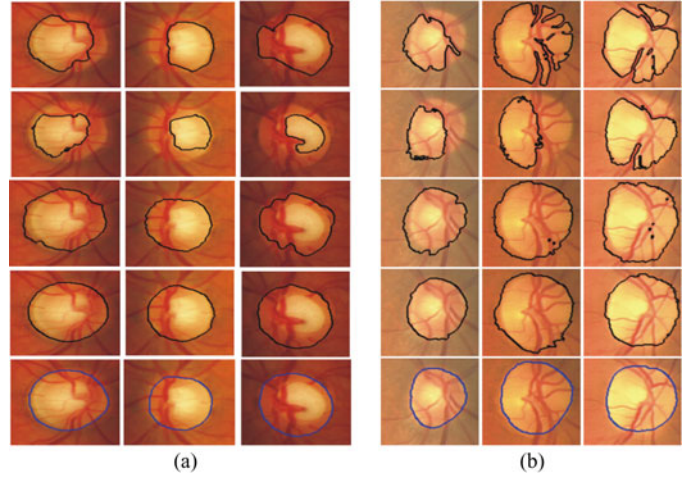


Fig. 14. (a) Optic disk segmentation results of DIARETDB1 images: first row topology cut, second row graph cut, third row compensation factor algorithm, fourth row MRF image reconstruction algorithm, and fifth row hand labeled. (b) Optic disk segmentation results of DRIVE images: first row topology cut, second row graph cut, third row compensation factor algorithm, fourth row MRF image reconstruction algorithm, and fifth row hand labeled.

our method. MAD is defined as

$$MAD(G_c, S_c) = \frac{1}{2} \left\{ \frac{1}{n} \sum_{i=1}^n d(g_{ci}, S) + \frac{1}{m} \sum_{i=1}^m d(s_{ci}, G) \right\} \quad (17)$$

where  $G_c$  and  $S_c$  are the contours of the segmented regions of the ground truth and our algorithm, respectively.  $d(a_i, B)$  is the minimum distance from the position of the pixel  $a_i$  on the contour  $A$  to the contour  $B$ . A good segmentation implies a high overlapping ratio and a low MAD value.

The sensitivity of our method on DIARETDB1 and DRIVE is defined as

$$\text{Sensitivity} = \frac{Tp}{Tp + Fn} \quad (18)$$

where  $Tp$  and  $Fn$  are the number of true positives and the number of false negatives, respectively. The sensitivity indicates the detection of the Fg pixels by the segmentation method.

Fig. 14(a) and (b) show the optic disk segmentation results of topology cut technique [38], traditional graph cut technique [24], and both our methods: the optic disk segmentation with the compensation factor and the optic disk segmentation with the MRF image reconstruction on DIARETDB1 and DRIVE, respectively. Considering the ground truth images, it is clear that both our methods perform better than alternative methods: topology cut technique [38] and traditional graph cut technique [24]. The topology cut technique achieved acceptable results in the brighter images, characterized by vessels that are more likely to belong to the Fg (similar intensity as the optic disk). However, the traditional graph cut technique tends to segment only the brightest region of the disk; this is due to the intrusion of the blood vessels in the optic disk region, which misguide the segmentation algorithm to follow a short path.

Table V shows the performance of our proposed methods with alternative methods on the DIARETDB1 images. The

TABLE V  
PERFORMANCE COMPARISON ON THE DIARETDB1 DATASET

Method	Average ORatio	Average MAD	Average Sensitivity
Topology cut [38]	0.3843	17.49	0.5530
Adaptive morphologic [14]	0.4365	8.31	—
Graph cut [24]	0.5403	10.74	0.7635
<b>Compensation Factor</b>	0.7594	6.18	0.8675
<b>MRF Image Reconstruction</b>	0.7850	6.55	0.8750

TABLE VI  
PERFORMANCE COMPARISON ON THE DRIVE DATASET

Method	Average ORatio	Average MAD	Average Sensitivity
Topology Cut [38]	0.5591	10.24	0.6512
Adaptive morphologic [14]	0.4147	5.74	—
Graph cut [24]	0.5532	9.97	0.7398
<b>Compensation Factor</b>	0.709	6.48	0.8464
<b>MRF Image Reconstruction</b>	0.8240	3.39	0.9819

compensation factor  $Vad$  and the MRF image reconstruction segmentation algorithms achieve the overlapping ratios of 0.7594 and 0.7850, and outperform the approaches in [14], [24], and [38]. However, considering the performance in terms of a mean absolute distance, MRF image reconstruction algorithm reaches the lowest value 6.55 and performs better than all the other methods. Both our methods achieve the highest average sensitivity with 87.50% for the MRF image reconstruction and 86.75% for the compensation factor  $Vad$  in 96.7% on the DIARETDB1 images.

Table VI shows the performance results of our methods with other alternative methods in terms of  $Oratio$ , MAD, and Sensitivity on DRIVE images. An overview of the segmentation results shows that our proposed methods achieved the highest overlapping ratio with the minimum MAD value compared to the traditional graph cut method [24] and the topology cut method [38], except for the adaptive morphologic method [14], which is marginally inferior to the compensation factor algorithm in terms of MAD. However, an increase in the overlapping ratio does not necessarily mean a decrease of MAD value. Thus, the value of MAD alone is not enough to measure the performance of segmentation results, but it provides a good reference of the contour matching with the ground truth contour reference.

For further performance comparison, we used the cumulative histogram to compare the overlapping ratio of our proposed method against topology Cut [38] and graph cut [24]. This is done by performing each segmentation method against the human expert hand labeled, and the cumulative histogram represents the frequency of the  $Oratio$  value. A perfect segmentation is achieved when the value of  $Oratio = 1$  and the area under the curve is equal to zero. Figs. 15 and 16 show the plots of the cumulative histograms of the overlapping ratio for topology cut [38] and graph cut [24], compensation factor and MRF image reconstruction on DIARETDB1 and DRIVE datasets, respectively. The overview of the graphs shows that the compensation factor and MRF image reconstruction methods achieve the minimum

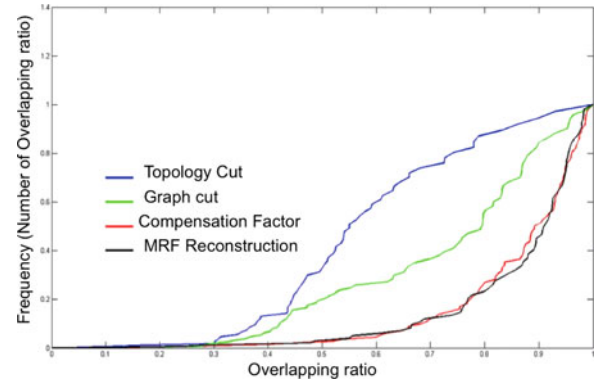


Fig. 15. Cumulative histogram for the overlapping ratio of DIARETDB1 images.

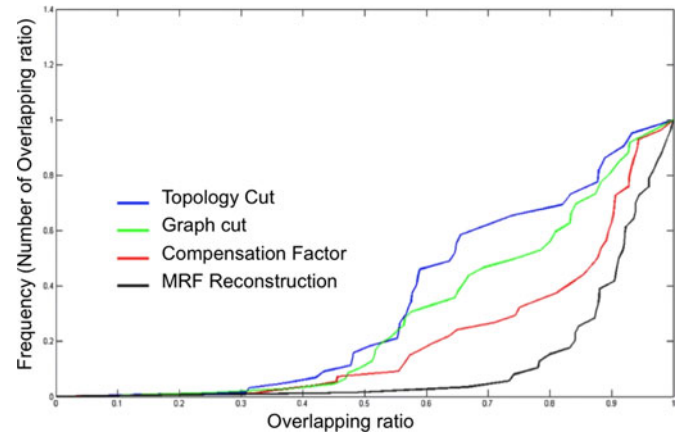


Fig. 16. Cumulative histogram for the overlapping ratio of DRIVE images.

area under the graph; hence, our method outperforms all other methods. In general, the MRF image reconstruction method reaches better results on DRIVE images, while the compensation factor method produces better segmentation results on the DIARETDB1 dataset.

Based on the assumption in Niemeijer *et al.* [39], which considers a minimum overlapping ratio  $Oratio > 50\%$  as a successful segmentation, the compensation factor algorithm with 86.52% success performs better on DRIVE than DIARETDB1 and the segmentation of MRF image reconstruction with 90.00% achieves better results than the compensation factor algorithm on DRIVE.

## VI. DISCUSSIONS AND CONCLUSION

We have presented a novel approach for blood vessels and optic disk segmentation in retinal images by integrating the mechanism of flux, MRF image reconstruction, and compensation factor into the graph cut method. The process also involves contrast enhancement, adaptive histogram equalization, binary opening, and distance transform for preprocessing.

We have evaluated the performance of vessel segmentation against ten other methods including human manual labeling on the STARE dataset and 15 other methods including human manual labeling on the DRIVE dataset. For the optic disk



segmentation, we have evaluated the performance of our method against three other methods on the DRIVE and DIARETDB1 datasets.

Tables II, III, and IV show performance comparison in terms of the average TPR, FPR, and ACC. According to these results, our vessel segmentation algorithm reaches acceptable results and outperforms all other methods in terms of average TPR on both STARE and DRIVE images. In terms of average accuracy, our method outperforms Hoover *et al.* [2], Martinez-Perez *et al.* [9], and Chaudhuri *et al.* [6] on STARE images. On DRIVE, it performs better than Jiang *et al.* [36], Cinsdikici *et al.* [35], Zana *et al.* [7], Garg *et al.* [31], Zhang *et al.* [29], and Martinez *et al.* [9]. Nevertheless, our method is marginally inferior to the methods presented by Staal *et al.* [5], Kaba *et al.* [27], Marin *et al.* [28], and Zhang *et al.* [29] on STARE, and Al-Rawi *et al.* [33], Ricci *et al.* [37], Mendonca *et al.* [3], Soares *et al.* [30], Marin *et al.* [28], and Staal *et al.* [5] on DRIVE. Although Soares *et al.* [30], Marin *et al.* [28], Staal *et al.* [5], and Ricci *et al.* [37] seem to achieve higher accuracy, as supervised techniques, they generally depend on the training datasets; thus to achieve excellent results, classifier retraining is required before performing any experimentation on new datasets. Further studies in [28] proved that these methods perform well when both training and testing are applied on the same dataset, but the performance deteriorates when the method is tested and trained on different datasets. Since these methods are sensitive to the training datasets, deploying them for practical use in retinal blood vessel segmentation would need further improvement as segmentation algorithms must work on retinal images taken under different conditions to be effective.

Our proposed method incorporates the prior knowledge of blood vessels to perform the segmentation, and it can be applied on retinal images from multiple sources and under different conditions without a need for training. This can be seen in the results achieved by this method on both the STARE and DRIVE datasets.

For the optic disk segmentation, Tables V and VI present the performance of our method on DIARETDB1 and DRIVE images. The results show that our methods of using the compensation factor and the MRF image reconstruction achieved the best overall performance. The results also show that the MRF image reconstruction algorithm outperforms the compensation factor algorithm by 2.56% and 11.5% on the DIARETDB1 and DRIVE images, respectively. However, it is important to notice that the MRF image reconstruction algorithm depends on the vessel segmentation algorithm; for example, if the vessel segmentation algorithm achieved a low performance on severely damaged retinal image, the reconstruction would not define a meaningful optic disk region, and hence the segmentation will fail.

Furthermore, the proposed method addresses one of the main issues in medical image analysis, “the overlapping tissue segmentation.” Since the blood vessels converse into the optic disk area and misguide the graph cut algorithm through a short path, breaking the optic disk boundary, to achieve good segmentation results, the MRF image reconstruction algorithm eliminates vessels in the optic disk area without any modification of the image

structures before segmenting the optic disk. On the other hand, the compensation factor incorporates vessels using local intensity characteristics to perform the optic disk segmentation. Thus, our method can be applied in other medical image analysis applications to overcome “the overlapping tissue segmentation.”

Our future research will be based on the segmentation of retinal diseases (lesions) known as “exudates” using the segmented structures of the retina (blood vessels and optic disk). Thus, a Bg template can be created using these structures. Then, this template can be used to perform the detection of suspicious areas (lesions) in the retinal images.

#### ACKNOWLEDGMENT

The authors would like to thank V. Kolmogorov for providing the software MaxFlow-v3.01 to compute the graph cut.

#### REFERENCES

- [1] K. Fritzsche, A. Can, H. Shen, C. Tsai, J. Turner, H. Tanenbaum, C. Stewart, B. Roysam, J. Suri, and S. Laxminarayan, “Automated model based segmentation, tracing and analysis of retinal vasculature from digital fundus images,” in *State-of-The-Art Angiography, Applications and Plaque Imaging Using MR, CT, Ultrasound and X-rays*. Boca Raton, FL, USA: CRC Press, 2003, pp. 225–298.
- [2] A. Hoover, V. Kouznetsova, and M. Goldbaum, “Locating blood vessels in retinal images by piecewise threshold probing of a matched filter response,” *IEEE Trans. Med. Imag.*, vol. 19, no. 3, pp. 203–210, Mar. 2000.
- [3] A. M. Mendonca and A. Campilho, “Segmentation of retinal blood vessels by combining the detection of centerlines and morphological reconstruction,” *IEEE Trans. Med. Imag.*, vol. 25, no. 9, pp. 1200–1213, Sep. 2006.
- [4] J. Soares, J. Leandro, R. Cesar, H. Jelinek, and M. Cree, “Retinal vessel segmentation using the 2-D gabor wavelet and supervised classification,” *IEEE Trans. Med. Imag.*, vol. 25, no. 9, pp. 1214–1222, Sep. 2006.
- [5] J. Staal, M. D. Abramoff, M. Niemeijer, M. A. Viergever, and B. van Ginneken, “Ridge-based vessel segmentation in color images of the retina,” *IEEE Trans. Med. Imag.*, vol. 23, no. 4, pp. 501–509, Apr. 2004.
- [6] S. Chaudhuri, S. Chatterjee, N. Katz, M. Nelson, and M. Goldbaum, “Detection of blood vessels in retinal images using two-dimensional matched filters,” *IEEE Trans. Med. Imag.*, vol. 8, no. 3, pp. 263–269, Sep. 1989.
- [7] F. Zana and J.-C. Klein, “Segmentation of vessel-like patterns using mathematical morphology and curvature evaluation,” *IEEE Trans. Image Process.*, vol. 10, no. 7, pp. 1010–1019, Jul. 2001.
- [8] L. Xu and S. Luo, “A novel method for blood vessel detection from retinal images,” *Biomed. Eng. Online*, vol. 9, no. 1, p. 14, 2010.
- [9] M. E. Martinez-Perez, A. D. Hughes, S. A. Thom, A. A. Bharath, and K. H. Parker, “Segmentation of blood vessels from red-free and fluorescein retinal images,” *Med. Image Anal.*, vol. 11, no. 1, pp. 47–61, 2007.
- [10] L. Zhou, M. S. Rzeszutarski, L. J. Singerman, and J. M. Chokreff, “The detection and quantification of retinopathy using digital angiograms,” *IEEE Trans. Med. Imag.*, vol. 13, no. 4, pp. 619–626, Dec. 1994.
- [11] C. Sinthanayothin, J. F. Boyce, H. L. Cook, and T. H. Williamson, “Automated localisation of the optic disk, fovea, and retinal blood vessels from digital colour fundus images,” *Brit. J. Ophthalmol.*, vol. 83, no. 8, pp. 902–910, 1999.
- [12] R. Chrastek, M. Wolf, K. Donath, H. Niemann, D. Paulus, T. Hothorn, B. Lausen, R. Lammer, C. Y. Mardin, and G. Michelson, “Automated segmentation of the optic nerve head for diagnosis of glaucoma,” *Med. Image Anal.*, vol. 9, no. 1, pp. 297–314, 2005.
- [13] J. Lowell, A. Hunter, D. Steel, A. Basu, R. Ryder, E. Fletcher, and L. Kennedy, “Optic nerve head segmentation,” *IEEE Trans. Med. Imag.*, vol. 23, no. 2, pp. 256–264, Feb. 2004.
- [14] D. Welfer, J. Scharcanski, C. Kitamura, M. D. Pizzol, L. Ludwig, and D. Marinho, “Segmentation of the optic disk in color eye fundus images using an adaptive morphological approach,” *Comput. Biol. Med.*, vol. 40, no. 1, pp. 124–137, 2010.
- [15] A. Aquino, M. E. Gegúndez-Arias, and D. Marín, “Detecting the optic disk boundary in digital fundus images using morphological, edge detection, and feature extraction techniques,” *IEEE Trans. Med. Imag.*, vol. 29, no. 11, pp. 1860–1869, Nov. 2010.

- [16] A. Salazar-Gonzalez, Y. Li, and X. Liu, "Optic disk segmentation by incorporating blood vessel compensation," in *Proc. IEEE SSCI, Int. Workshop Comput. Intell. Med. Imag.*, 2011, pp. 1–8.
- [17] A. G. Salazar-Gonzalez, Y. Li, and X. Liu, "Retinal blood vessel segmentation via graph cut," in *Proc. IEEE 11th Int. Conf. Contr. Autom. Robot. Vis.*, 2010, pp. 225–230.
- [18] A. Salazar-Gonzalez, Y. Li, and D. Kaba, "Mrf reconstruction of retinal images for the optic disk segmentation," in *Health Information Science*. New York, NY, USA: Springer-Verlag, 2012, pp. 88–99.
- [19] A. G. S. Gonzalez, "Structure analysis and lesion detection from retinal fundus images," Ph.D. dissertation, Dept. Comput. Sci., Brunel Univ., West London, U.K., 2011.
- [20] D. Wu, M. Zhang, and J. Liu, "On the adaptive detection of blood vessels in retinal images," *IEEE Trans. Biomed. Eng.*, vol. 53, no. 2, pp. 341–343, Feb. 2006.
- [21] Y. Y. Boykov and M.-P. Jolly, "Interactive graph cuts for optimal boundary & region segmentation of objects in N-D images," in *Proc. IEEE 8th Int. Conf. Comput. Vis.*, 2001, vol. 1, pp. 105–112.
- [22] S. Vicente, V. Kolmogorov, and C. Rother, "Graph cut based image segmentation with connectivity priors," in *Proc. IEEE Conf. Comput. Vis. Pattern Recogn.*, 2008, vol. 1, pp. 1–8.
- [23] V. Kolmogorov and Y. Boykov, "What metrics can be approximated by geo-cuts, or global optimization of length/area and flux," in *Proc. 10th IEEE Int. Conf. Comput. Vis.*, 2005, vol. 1, pp. 564–571.
- [24] Y. Boykov and G. Funka-Lea, "Graph cuts and efficient N-D image segmentation," *Int. J. Comput. Vis.*, vol. 70, no. 2, pp. 109–131, 2006.
- [25] A. Efros and T. Leung, "Texture synthesis by non-parametric sampling," in *Proc. IEEE Int. Conf. Comput. Vis.*, 1999, pp. 1033–1038.
- [26] T. Kauppi, V. Kalesnykiene, J. Kamarainen, L. Lensu, I. Sorri, A. Raninen, R. Voutilainen, H. Uusitalo, H. Kalviainen, and J. Pietila, "Diaretdb1 diabetic retinopathy database and evaluation protocol," in *Proc. Brit. Mach. Vis. Conf.*, 2007, pp. 1–10.
- [27] D. Kaba, A. G. Salazar-Gonzalez, Y. Li, X. Liu, and A. Serag, "Segmentation of retinal blood vessels using gaussian mixture models and expectation maximisation," in *Health Information Science*. New York, NY, USA: Springer-Verlag, 2013, pp. 105–112.
- [28] D. Marín, A. Aquino, M. E. Gegúndez-Arias, and J. M. Bravo, "A new supervised method for blood vessel segmentation in retinal images by using gray-level and moment invariants-based features," *IEEE Trans. Med. Imag.*, vol. 30, no. 1, pp. 146–158, Jan. 2011.
- [29] B. Zhang, L. Zhang, L. Zhang, and F. Karray, "Retinal vessel extraction by matched filter with first-order derivative of gaussian," *Comput. Biol. Med.*, vol. 40, no. 4, pp. 438–445, 2010.
- [30] J. V. Soares, J. J. Leandro, R. M. Cesar, H. F. Jelinek, and M. J. Cree, "Retinal vessel segmentation using the 2-D gabor wavelet and supervised classification," *IEEE Trans. Med. Imag.*, vol. 25, no. 9, pp. 1214–1222, Sep. 2006.
- [31] S. Garg, J. Sivaswamy, and S. Chandra, "Unsupervised curvature-based retinal vessel segmentation," in *Proc. IEEE 4th IEEE Int. Symp. Biomed. Imag.: Nano Macro*, 2007, pp. 344–347.
- [32] R. Perfetti, E. Ricci, D. Casali, and G. Costantini, "Cellular neural networks with virtual template expansion for retinal vessel segmentation," *IEEE Trans. Circuits Syst. II, Exp. Briefs.*, vol. 54, no. 2, pp. 141–145, Feb. 2007.
- [33] M. Al-Rawi, M. Qutaishat, and M. Arrar, "An improved matched filter for blood vessel detection of digital retinal images," *Comput. Biol. Med.*, vol. 37, no. 2, pp. 262–267, 2007.
- [34] M. Niemeijer, J. Staaf, B. van Ginneken, M. Loog, and M. D. Abramoff, "Comparative study of retinal vessel segmentation methods on a new publicly available database," in *Proc. SPIE Med. Imag. Int. Soc. Opt. Photon.*, 2004, pp. 648–656.
- [35] M. G. Cinsdikici and D. Aydın, "Detection of blood vessels in ophthalmoscope images using mf/ant (matched filter/ant colony) algorithm," *Comput. Methods Prog. Biomed.*, vol. 96, no. 2, pp. 85–95, 2009.
- [36] X. Jiang and D. Mojon, "Adaptive local thresholding by verification-based multithreshold probing with application to vessel detection in retinal images," *IEEE Trans. Pattern Anal. Mach. Intell.*, vol. 25, no. 1, pp. 131–137, Jan. 2003.
- [37] E. Ricci and R. Perfetti, "Retinal blood vessel segmentation using line operators and support vector classification," *IEEE Trans. Med. Imag.*, vol. 26, no. 10, pp. 1357–1365, Oct. 2007.
- [38] Y. Zeng, D. Samaras, W. Chen, and Q. Peng, "Topology cuts: A novel min-cut/max-flow algorithm for topology preserving segmentation in n-d images," *J. Comput. Vis. Image Understand.*, vol. 112, no. 1, pp. 81–90, 2008.

- [39] M. Niemeijer, M. D. Abramoff, and B. Van Ginneken, "Segmentation of the optic disk, macula and vascular arch in fundus photographs," *IEEE Trans. Med. Imag.*, vol. 26, no. 1, pp. 116–127, Jan. 2007.



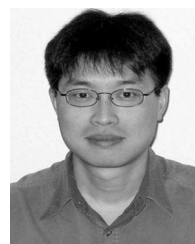
**Ana Salazar-Gonzalez** was born in Irapuato, Guanajuato, Mexico, in 1979. She received the B.S. degree in electronics engineering in 2003, and the M.S. degree in signal processing from the Universidad de Guanajuato, Guanajuato, Mexico, in 2006. She received the Ph.D. degree in computer science from Brunel University, London, U.K., in 2012.

Since 2003, she has been dedicated to the design and development of image processing systems. Her research interests include medical image analysis, OCR systems, and image processing for security documents under different wavelength lights. Currently, she is an Engineer at Access IS, Reading, U.K., designing and developing OCR systems and protocols of validation for security documents (passports, visas, ID cards, driving licenses, etc.).



**Djibril Kaba** received the M.Eng. and B.Eng. degrees in electronics engineering from Kings' College University, London, U.K., in 2010. He is currently working toward the Ph.D. degree in the Department of Computer Science, Brunel University, West London, U.K.

From 2010 to 2011, he worked as a Business Analyst for ITSeven, London, U.K. Since 2011, he has been a Teaching Assistant in the Department of Computer Science, Brunel University, London, U.K. His research interests include computer vision, image processing, pattern recognition, medical image analysis, and machine learning.



**Yongmin Li** received the M.Eng. and B.Eng. degrees in control engineering from Tsinghua University, Beijing, China, in 1990 and 1992, respectively, and the Ph.D. degree in computer vision from Queen Mary University of London, London, U.K., in 2001.

Between 2001 and 2003, he worked as a Research Scientist at the British Telecom Laboratories, Suffolk, U.K. He is currently a Senior Lecturer in the Department of Computer Science, Brunel University, West London, U.K. His current research interests include automatic control, nonlinear filtering, computer vision, image processing, video analysis, medical imaging, machine learning, and pattern recognition.



**Xiaohui Liu** received the B.Eng. degree in computing from Hohai University, Nanjing, China, in 1982 and the Ph.D. degree in computer science from Heriot-Watt University, Edinburgh, U.K., in 1988.

He is currently a Professor of computing at Brunel University, West London, U.K., where he directs the Centre for Intelligent Data Analysis, conducting interdisciplinary research concerned with the effective analysis of data. He also a Professor of computing at King Abdulaziz University, Jeddah 21589, Saudi Arabia. He is a Chartered Engineer, Life Member of the Association for the Advancement of Artificial Intelligence, Fellow of the Royal Statistical Society, and Fellow of the British Computer Society. He has over 100 high quality journal publications in biomedical informatics, complex systems, computational intelligence, and data mining. His H-index is over 40.